ACS APPLIED MATERIALS & INTERFACES

RESEARCH ARTICLE

www.acsami.org

Graphene-Encapsulated Hollow Fe_3O_4 Nanoparticle Aggregates As a High-Performance Anode Material for Lithium Ion Batteries

Dongyun Chen,[†,‡] Ge Ji,[†] Yue Ma,[†] Jim Yang Lee,[*,†] and Jianmei Lu[*,‡]

[†]Department of Chemical & Biomolecular Engineering, Faculty of Engineering, National University of Singapore, 10 Kent Ridge Crescent, Singapore, 119260; Tel: +65 65162186.

[‡]Key Laboratory of Organic Synthesis of Jiangsu Province, Key Laboratory of Functional Materials for Environment Protection, College of Chemistry, Chemical Engineering and Materials Science, Soochow University, Suzhou, China, 215123; Tel: +86 512 65880367.

Supporting Information

ABSTRACT: Graphene-encapsulated ordered aggregates of Fe_3O_4 nanoparticles with nearly spherical geometry and hollow interior were synthesized by a simple self-assembly process. The open interior structure adapts well to the volume change in repetitive Li^+ insertion and extraction reactions; and the encapsulating graphene connects the Fe_3O_4 nanoparticles electrically. The structure and morphology of the graphene-Fe_3O_4 composite were confirmed by X-ray diffraction, scanning electron microscopy, and high-resolution transmission microscopy. The electrochemical performance of the composite for reversible Li^+ storage was evaluated by cyclic voltammetry and constant current charging and discharging. The results showed a high and nearly unvarying specific capacity for 50 cycles. Furthermore, even after 90 cycles of charge and discharge at different current densities, about 92% of the initial capacity at 100 mA g^{-1} was still recoverable, indicating excellent cycle stability. The graphene-Fe_3O_4 composite is therefore a capable Li^+ host with high capacity that can be cycled at high rates with good cycle life. The unique combination of graphene encapsulation and a hollow porous structure definitely contributed to this versatile electrochemical performance.

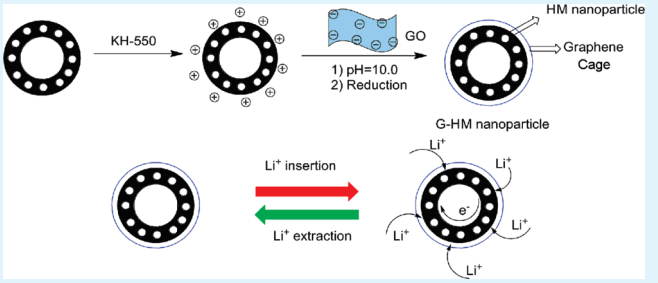

KEYWORDS: Fe_3O_4, graphene, anode material, lithium ion batteries

1. INTRODUCTION

Lithium ion batteries are undoubtedly the most advanced rechargeable batteries on the market today. There is increasing interest in deploying them for electric vehicle and distributed power generation applications.[1] The specifications for these large scale applications are clearly more demanding, requiring substantial improvements in the capacity, rate performance, and cycle life of the cathode and anode materials.[2−4] Electrochemically active transition metal oxide nanoparticles, with their high theoretical capacity, are one of the candidates for next-generation anode materials.[5−11] Among them, Fe_3O_4 has shown the most promise because of its environmental benignity, low cost, and natural abundance.[12−16] During charging, the transition metal oxide is reduced to small metallic clusters and the released oxygen combines with incoming Li^+ to form Li_2O. This reaction causes significant volume excursions in the material which can weaken the electrical connectivity between the active particles.[17,18] Continuing cycling aggravates the situation leading eventually to anode disintegration and rapid capacity fading.

There have been several strategies used to mitigate the instability caused by volume excursions. One of them is to assemble the active nanoparticles into a hollow mesoscale structure; using the free volume in the hollow structure to cushion the volume changes.[19−21] The porosity between the nanoparticles can also improve the accessibility of the host material to lithium ions; and shortens the diffusion path of the latter.[22−24] The last aspect of the material design is electrical integration of the active particles; which is often carried out by the chemical vapor deposition (CVD) of carbon at high temperatures under a reducing atmosphere. However, the carbon deposited as such may not have the best electrical conductivity.[25] Conversely the best conditions for conductive carbon formation may alter the nanoparticle structure, and hence their reactivity. In addition, there is no control in the percolation of the particle porosity by carbon. The proximity of carbon to the active particles may not be optimal to provide the lowest contact resistance.

Graphene, an alternative form of conductive carbon, may provide as a solution. Graphene is monolayer graphite endowed with a strong suite of properties such as good chemical stability, excellent electrical conductivity ($\sigma = 1 \times 10^6$ ohm^{-1} cm^{-1}) and some unique electronic properties (e.g., room temperature quantum Hall effect and massless electron transport properties).[26,27] Because graphene can be introduced without a CVD procedure, the graphene modification of nanoparticles may circumvent the

Received: May 12, 2011
Accepted: July 12, 2011
Published: July 12, 2011

Scheme 1. Schematic Illustration of the Fabrication Process and the Structure of the Resulting G-HM Composite Particles

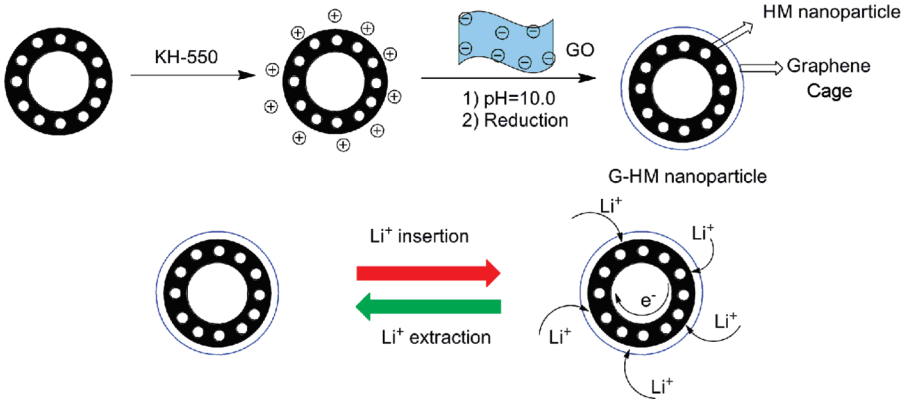

potential damages to the nanoparticle structure and properties caused by CVD. Hence, there have been a few recent studies on restacking the graphene sheets in the presence of discrete guest nanoparticles or corresponding organometallic precursors for lithium ion battery applications, with the aim of combining the electrochemical properties of both.[28−36] During cycling, however, the nanoparticles in the hybrid structure were found to aggregate strongly because the nonoptimal contact between the graphene sheets and the active nanoparticles could not produce an adequate opposing force to aggregation. Consequently the storage capacity of the active particles decreased precipitously after a few cycles. We propose here a solution to maintain the dispersion of nanoparticles in graphene by forming nanoparticles into aggregates and by encapsulating the aggregates with individual graphene cages.

In this study, we combine the unique properties of graphene sheets and a hollow assembly of nanoparticles to simultaneously provide a large reversible Li^+ storage capacity, good rate performance, and long cycle life. A simple self-assembly process driven by electrostatic interaction was used to generate graphene-encapsulated hollow Fe_3O_4 nanoparticle aggregates (G-HM, short for graphene-encapsulated hollow magnetite particles) (see Scheme 1). In this process, graphene oxide and HM nanoparticle aggregates were first modified to acquire negative and positive charged, respectively. The assembly was carried out under very mild reaction conditions and consequently perturbations to the intrinsic properties of the HM nanoparticles could be kept to a minimum. The G-HM composite particles synthesized as such showed remarkable cycle stability as well as lithium storage performance compared to the pristine HM nanoparticles or a mixture of graphene and HM particles. The graphene modification of porous nanoparticle aggregates is therefore a viable and facile approach to prepare high-performance anode materials for the lithium ion batteries.

2. EXPERIMENTAL SECTION

2.1. Synthesis of Hollow Porous Fe_3O_4 Nanoparticles. Monodisperse HM nanoparticles were synthesized by simple one-pot hydrothermal method. Typically, 2.06 g (8 mmol) of sodium citrate, 0.72 g (12 mmol) of urea, and 1.08 g (4 mmol) of ferric chloride hexahydrate were first dissolved in 50 mL ethylene glycol. Then 600 mg polyacrylamide ($M_w = 1 \times 10^4$ g mol^{-1}) aqueous solution (50 wt %) was added under stirring to form a green clear solution which was then transferred to a Teflon-lined stainless steel autoclave. The autoclave was sealed and heated at 200 °C for 8 h and then cooled to room temperature naturally. The HM nanoparticles so obtained were black in color, and were washed several times with ethanol and deionized water before drying in vacuum at 60 °C for 24 h.

2.2. Synthesis of Graphene-Encapsulated Hollow Porous Fe_3O_4 (G-HM) Nanoparticles. The encapsulation of HM nanoparticles within graphene sheets were synthesized according to the literature with some modifications.[37] Graphene oxide (GO) was first synthesized from natural graphite flakes.[38] The HM nanoparticles were surface modified with amino groups as follows: 100 μL of 3-aminopropyltriethoxysilane (KH550) was added dropwise to the HM nanoparticle solution in toluene (50 mL) and stirred for 24 h. The resulting aminated nanoparticles were recovered magnetically and washed with ethanol. The aminated nanoparticles (40 mg) and graphene oxide (9 mg) were then separately dispersed in sodium hydroxide aqueous solution (300 mL, pH 10.0) by sonication. The two solutions were then mixed under mild stirring. GO-HM nanoparticles were formed by the electrostatic interaction between these two oppositely charged nanomaterials. Two h later, 3 mL of hydrazine aqueous solution (35 wt %) was added to the GO-HM suspension, and stirring was continued overnight. The reduced G-HM nanocomposites were centrifugally separated, washed, and dried as mentioned before.

2.3. Characterization of G-HM Nanocomposites. The morphology and structure of the samples were characterized by powder X-ray diffraction (XRD) on a Shimadu XRD-6000 using Cu Kα radiation; by field-emission scanning electron microscopy and scanning transmission electron microscopy (FESEM/STEM) on a JEOL JSM-6700F operating at 5 kV; by scanning electron microscopy and energy-dispersive X-ray spectroscopy (SEM/EDX) on a JEOL JSM-840 operating at 15 kV; and by transmission electron microscopy and selected area electron diffraction (TEM/SAED) on a JEOL JEM-2010F operating at 200 kV.

2.4. Electrochemical Measurements. The electrochemical properties of the nanomaterials were evaluated by galvanostatic charging and discharging. The active anode material (G-HM, 80 wt %), conducting additive (10 wt %, Super-P carbon black, Timcal) and polyvinylidene fluoride (10 wt %, PVDF) binder were mixed in N-methylpyrrolidone (NMP) to form a homogeneous slurry. The slurry was then coated on a copper foil current collector and dried in vacuum at 120 °C. Electrochemical test cells were assembled in an argon-filled glovebox using the coated copper foil as the working electrode, a lithium metal foil as the counter/reference electrode, and 1 M solution of LiPF6 in a 50:50 w/w mixture of ethylene carbonate (EC) and diethyl carbonate (DEC) as the electrolyte. The cells were discharged and charged galvanostatically at various current densities over the voltage window of 5 mV to 3 V on a Maccor series 2000 battery tester at room temperature.

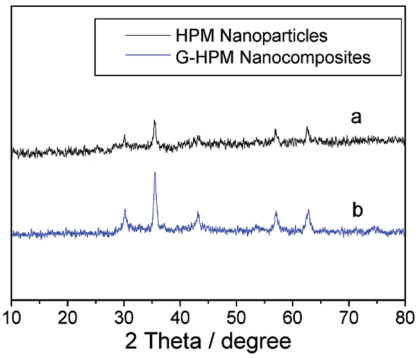

Figure 1. XRD patterns of the as-synthesized HM nanoparticles and G-HM nanocomposites.

3. RESULTS AND DISCUSSION

3.1. Characterization of the G-HM Microstructure. An overview of the chemical route to the G-HM composite particles is shown in Scheme 1. The HM nanoparticle aggregates were first prepared by a one-pot hydrothermal synthesis. Then, they were modified to be positively charged by KH550, and electrostatically assembled with negatively charged graphene oxide in alkaline solution. Finally, chemical reduction in aqueous hydrazine solution (35 wt %) was used to reduce graphene oxide to graphene, thereby finalizing the packaging of the HM particles in individual graphene cages.

The crystal structures of as-prepared HM and G-HM were determined by X-ray diffraction (XRD) spectrometry. As shown in Figure 1a, all the peaks of HM could be indexed to magnetite based on their good agreement with JCPDS Card 75−0033. No peaks from γ-Fe_2O_3 were found in the pattern, indicating that the one-pot hydrothermal synthesis only produced phase-pure magnetite HM particles (see Figures S1 and S2 in the Supporting Information). The use of citrate in the hydrothermal synthesis was important to ensuring the formation of phase-pure nanoparticles. At elevated temperatures, citrate reduced Fe^{3+} to Fe^{2+}. At the same time, urea was hydrolyzed to ammonia and carbon dioxide to provide an alkaline environment for the formation of ferric and ferrous hydroxides. The mixed hydroxides were then dehydrated to form Fe_3O_4 nanoparticles, whereas the hydrothermal conditions induced their assembly into aggregated particles with a hollow interior and porous shell. The XRD pattern of G-HM particles is shown in Figure 1b. There were no significant diffractions from the graphene sheets suggesting that the graphene sheets had distributed uniformly as the encapsulant for the magnetite nanoparticle aggregates. Inductively coupled plasma atomic emission spectroscopy (ICP-AES) measured the weight fraction of the HM particles in the G-HM composite particles to be as high as 90.2%. The high content of the active materials ensured that the overall capacity would not be lowered by the dead weight effect of graphene.

The size and morphology of the HM particles before and after graphene sheet encapsulation were examined by SEM and TEM. Figure 2a shows a typical SEM image of the HM particles. The particles were spherical in shape and nearly monodisperse in size with an average diameter of ~220 nm. The particle surface was rough in texture which, upon closer scrutiny, revealed an ordered assembly of nanoparticles. The void in nanoparticle packing gave rise to the porosity in the overall assembled structure. The hollow interior of the assembly was confirmed by TEM imaging which

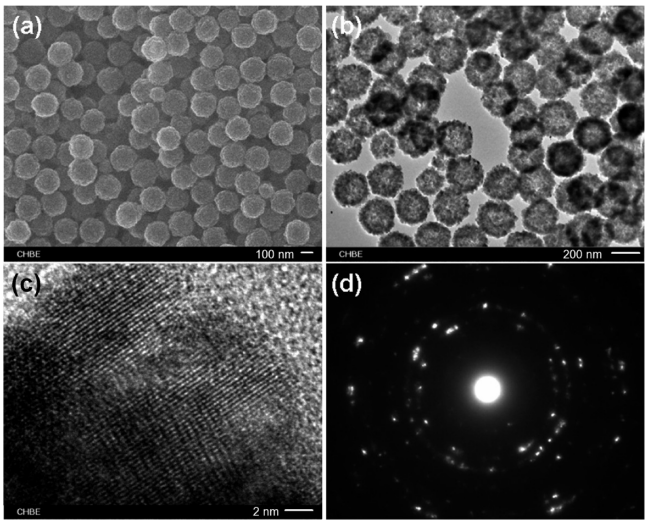

Figure 2. Typical (a) SEM, (b) TEM, (c) HRTEM, and (d) SAED images of HM particles.

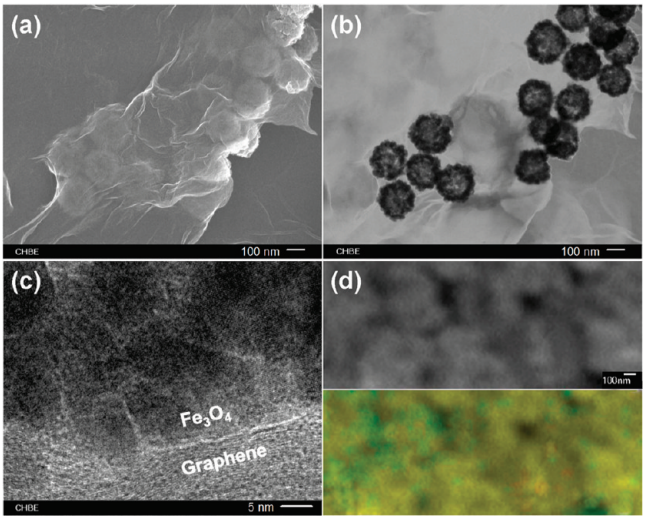

Figure 3. Typical (a) FESEM, (b) STEM, (c) HRTEM images, and (d) elemental maps (carbon (green), iron (red), iron + carbon (yellow) of G-HM composite particles).

detected strong contrast between the darker edges and the paler central region (Figure 2b). High-resolution TEM (HRTEM) and SAED analyses were then used to characterize the surface structure of the nanoparticle aggregates. The HRTEM image in Figure 2c shows well-resolved atomic lattice fringes which are characteristic of a polycrystalline material; and all of the diffraction rings in the SAED pattern of Figure 2d are indexable to magnetite. The SEM and TEM analyses of HM nanoparticles therefore confirmed the formation of Fe_3O_4 nanoparticle aggregates with a hollow interior and porous shell by the one-pot hydrothermal synthesis.

The microstructure of the G-HM composite particles is shown in Figure 3a−d. FESEM and STEM imaging of the same area (Figure 3a,b) shows a uniform distribution of HM nanoparticle aggregates in the graphene sheets with the overall appearance of beetles caught in a cobweb. In addition each nanoparticle aggregate was also caged by continuous graphene sheets. The thinness

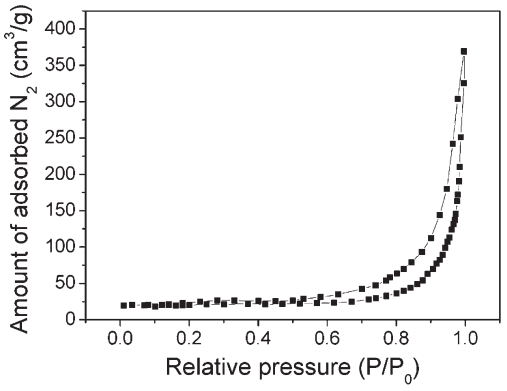

Figure 4. Nitrogen adsorption/desorption isotherms of the G-HM composite particles.

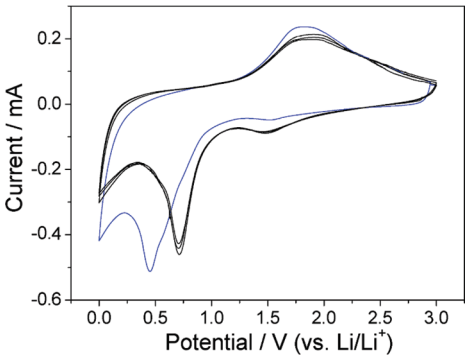

Figure 5. Cyclic voltammograms of the G-HM nanocomposites at a scan rate of 0.1 mV s^{-1} for four cycles (1st cycle in blue).

and the flexibility of the graphene sheets are believed to be the reason for the conformal encapsulation of the particle aggregates and their attachment to an interconnecting graphene web. The HRTEM image in Figure 3c corroborates the presence of graphene sheets on the nanoparticle aggregates forming individual graphene cages. EDX Elemental mapping was used to evaluate the distributions of iron and carbon throughout the entire area. Figure 3d confirms the uniform dispersion of HM particles in the G-HM composite particles.

The porosity of the G-HM composite particles was characterized by nitrogen adsorption−desorption isotherm measurements. The Brunauer-Emmet-Teller (BET) specific surface area and pore volume calculated from such measurements (Figure 4) were 132 m^2 g^{-1} and 0.39 cm^3 g^{-1} respectively, significantly higher than those of the pristine HM nanoparticles (see Figure S3 in the Supporting Information, 83 m^2 g^{-1} and 0.28 cm^3 g^{-1}, respectively) and iron oxide nanoparticles reported elsewhere.[14,39] The high specific surface area and pore volume could be attributed to the porosity of the HM nanoparticle aggregates as well as to the formation of secondary pores between HM nanoparticle aggregates and graphene sheets. This hypothesis was confirmed by the morphology shown in the SEM and TEM images. The porosity and the packaging of the HM nanoparticles in individual graphene cages could shorten the diffusion paths of Li^+ and electrons, and more effectively buffer the volume changes during Li^+ insertion and extraction reactions. All of these could contribute to improvements in lithium storage performance and cycle stability.

3.2. Electrochemical Properties of G-HM. The value of G-HM as a potential lithium-ion anode material was first evaluated by cyclic voltammetry (CV) in the 0 to 3.0 V voltage range at 0.1 mV·s^{-1}. Figure 5 shows the reduction and oxidation peaks in the first complete scan. The peak in the cathodic scan at 0.48 V could be attributed to the reduction of Fe_3O_4 to Fe^0 and the irreversible decomposition of the electrolyte.[40] The anodic peak at 1.78 V in the reverse anodic scan corresponds to the reversible oxidation of Fe^0. The redox reaction of Fe could support 8 mols of Li^+ insertion/extraction per formula weight of Fe_3O_4, thereby providing a reversible lithium storage capacity significantly higher than that of commercial graphite anode (372 mA h g^{-1}). In subsequent anodic and cathodic scans, both the peak current and the integrated area intensity were nearly unchanged from cycle to cycle, indicating that there was almost no capacity loss during charging. The CV measurements therefore indicated good electrochemical activity and stability of the G-HM composite particles.

Constant current charging and discharging at 100 mA g^{-1} in the 0 to 3.0 V window was performed next. As shown in panels a and b in Figure 6, the first discharge/charge curves of G-HM are very similar to those of HM, suggesting that the chemical nature of the HM particles had not been altered by graphene modification. The difference in second cycle discharge/charge curves from the first could be attributed to the formation of solid electrolyte interface and the reaction of lithium ions with the functional groups on the graphene sheets. In subsequent cycles, the capacity of HM particles decreased with each cycle while G-HM showed excellent capacity retention. This is indication of the contribution of the graphene sheets to stabilizing the electrochemical activity of the anode material, which corroborates the findings from the CV measurements.

The excellent cycling performance and high reversible capacity of the G-HM composite particles can certainly be credited to the graphene modification. In order to confirm that the good performance was not merely due to a physical blending effect, the G-HM particles were also compared to a physical mixture of graphene and HM particles of the same overall composition, G (9.8%)/HM (90.2%) and unmodified HM nanoparticles in longer-term cycling tests conducted at 100 mA·g^{-1} (Figure 6c). The comparison clearly showed the rapid decrease in the capacities of the G/HM mixture and pristine HM particles from 772 and 760 mA h g^{-1} to 392 and 203 mA h g^{-1}, respectively. On the contrary, the reversible capacity of G-HM composite, which stabilized to a high of around 900 mA h g^{-1} after the first two cycles, was practically unchanged throughout the 50 cycles. The nearly constant high specific reversible capacity was contributed not only by the presence of graphene but also by the form of their existence (as a networking medium which preserves the electrical connectivity of the HM particles despite the volume changes in the Li insertion and extraction reactions). The physical mixture of G (9.8%)/HM (90.2%) could not offer the same extent of integration. In addition, TEM examination of the morphology of G-HM and pristine HM particles after 10 discharge/charge cycles (see Figure S4 in the Supporting Information) showed insignificant changes in the former but partial pulverization of the latter into smaller nanoparticles. Hence graphene encapsulation of the HM particles has helped to increase the resilience of HM to cycling.

The rate performance of G-HM was also investigated. The composite particles were cycled from 50 to 800 mA g^{-1} in steps and returned to 100 mA g^{-1} Figure 6d shows that G-HM cycled well at each of these current densities. 58% of the capacity at 50 mA g^{-1} could be retained even when the current density was

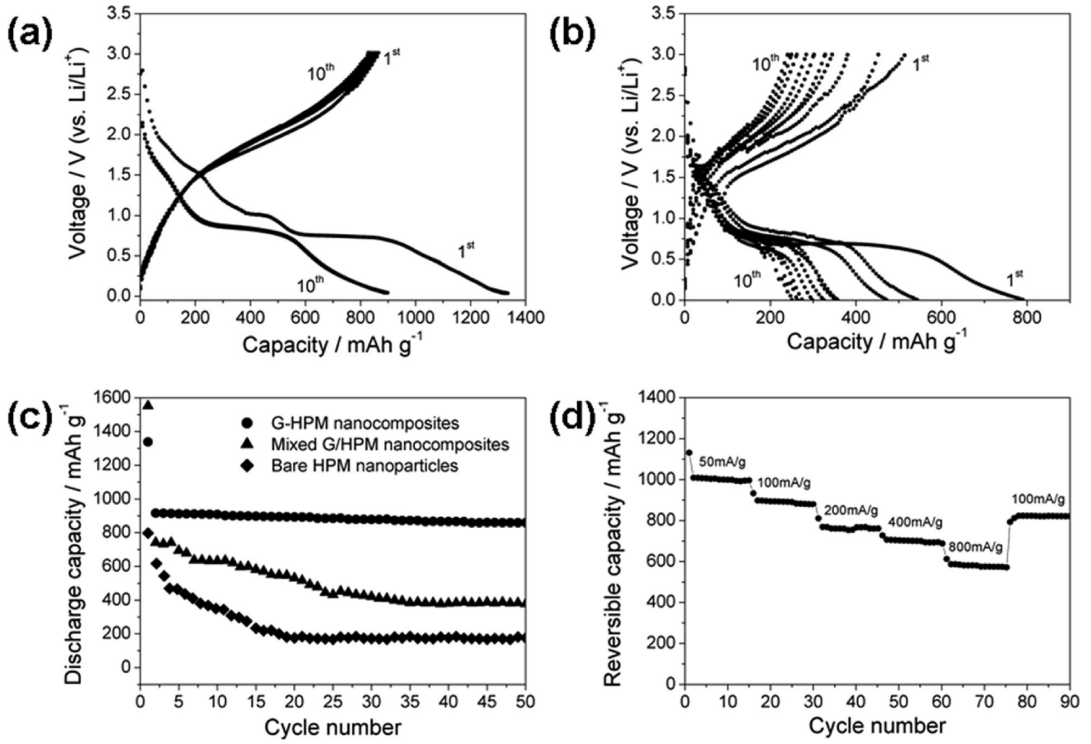

Figure 6. First ten cycle discharge/charge curves of (a) G-HM composite particles and (b) unmodified HM nanoparticle aggregates measured at a current density of 100 mA g^{-1}. (c) Comparison of cycle performance of G-HM, mixture of graphene and HM particles, and pristine HM nanoparticles at 100 mA g^{-1}. (d) Cycling performance of G-HM composite particles at different current densities.

increased to 800 mA g^{-1}, demonstrating excellent rate performance. After 60 cycles of charge and discharge at various current densities, a specific capacity of 832 mA h g^{-1} (about 92% of the capacity at 100 mA·g^{-1}) could still be obtained at 100 mA g^{-1}, indicating very good cycling stability of the electrode. These results confirmed that a high specific reversible capacity, good cycling stability, and excellent rate performance are all simultaneously possible in G-HM.

4. CONCLUSIONS

In conclusion, graphene-encapsulated Fe_3O_4 nanoparticle aggregates with hollow interior were fabricated by a two-step process involving hydrothermal synthesis and postsynthesis self-assembly under very mild reaction conditions. The composite particles displayed a stable high specific reversible capacity of around 900 mA h g^{-1}, which was nearly unvarying over 50 cycles. Moreover, even after 90 cycles of charge and discharge at different current densities, a specific capacity of 832 mA h g^{-1} at 100 mA g^{-1} was still possible, indicating excellent cycling stability of this anode material.

■ ASSOCIATED CONTENT

Supporting Information. FT-IR, XPS, and BET analysis results of HM; TEM images of G-HM and HM after discharge/charge cycles. This material is available free of charge via the Internet at http://pubs.acs.org.

■ AUTHOR INFORMATION

Corresponding Author

*E-mail: cheleejy@nus.edu.sg (J.Y.L.); lujm@suda.edu.cn (J.L.).

■ ACKNOWLEDGMENT

The attachment of D.C. to the National University of Singapore is partially financially supported by the China Scholarship Council (CSC).

■ REFERENCES

(1) Tollefson, J. *Nature* **2008**, *456*, 436–440.
(2) Tarascon, J. M.; Armand, M. *Nature* **2001**, *414*, 359–367.
(3) Ban, C.; Wu, Z.; Gillaspie, D. T.; Chen, L.; Yan, Y.; Blackburn, J. L.; Dillon, A. C. *Adv. Mater.* **2010**, *22*, E145–E149.
(4) Guo, Y. G.; Hu, Y. S.; Sigle, W.; Maier, J. *Adv. Mater.* **2007**, *19*, 2087–2091.
(5) Poizot, P.; Laruelle, S.; Grugeon, S.; Dupont, L.; Tarascon, J. M. *Nature* **2000**, *407*, 496–499.
(6) Nam, K. T.; Kim, D. W.; Yoo, P. J.; Chiang, C. Y.; Meethong, N.; Hammond, P. T.; Chiang, Y. M.; Belcher, A. M. *Science* **2006**, *312*, 885–888.
(7) Lou, X. W.; Deng, D.; Lee, J. Y.; Feng, J.; Archer, L. A. *Adv. Mater.* **2008**, *20*, 258–262.
(8) Zhi, L. J.; Hu, Y. S.; El Hamaoui, B.; Wang, X.; Lieberwirth, I.; Kolb, U.; Maier, J.; Müllen, K. *Adv. Mater.* **2008**, *20*, 1727–1731.
(9) Li, Y. G.; Tan, B.; Wu, Y. Y. *Nano Lett.* **2008**, *8*, 265–270.
(10) Chen, J.; Xu, L. N.; Li, W. Y.; Gou, X. L. *Adv. Mater.* **2005**, *17*, 582–586.
(11) Reddy, M. V.; Yu, T.; Sow, C. H.; Shen, Z. X.; Lim, C. T.; Rao, G. V. S.; Chowdari, B. V. R. *Adv. Funct. Mater.* **2007**, *17*, 2792–2799.
(12) Piao, Y.; Kim, H. S.; Sung, Y. E.; Hyeon, T. *Chem. Commun.* **2010**, *46*, 118–120.
(13) Taberna, P. L.; Mitra, S.; Poizot, P.; Simon, P.; Tarascon, J. M. *Nat. Mater.* **2006**, *5*, 567–573.
(14) Zhou, G.; Wang, D. W.; Li, F.; Zhang, L.; Li, N.; Wu, Z. S.; Wen, L.; Lu, G. Q.; Cheng, H. M. *Chem. Mater.* **2010**, *22*, 5306–5313.

(15) Lian, P.; Zhu, X.; Xiang, H.; Li, Z.; Yang, W.; Wang, H. *Electrochim. Acta* **2010**, *56*, 834–840.
(16) Yuan, S. M.; Li, J. X.; Yang, L. T.; Su, L. W.; Liu, L.; Zhou, Z. *ACS Appl. Mater. Interfaces* **2011**, *3*, 705–709.
(17) Muraliganth, T.; Murugan, A. V.; Manthiram, A. *Chem. Commun.* **2009**, *47*, 7360–7362.
(18) He, Y.; Huang, L.; Cai, J. S.; Zheng, X. M.; Sun, S. G. *Electrochim. Acta* **2010**, *55*, 1140–1144.
(19) Deng, D.; Lee, J. Y. *Chem. Mater.* **2008**, *20*, 1841–1846.
(20) Lou, X. W.; Li, C. M.; Archer, L. A. *Adv. Mater.* **2009**, *21*, 2536–2539.
(21) Yang, S.; Feng, X.; Zhi, L.; Cao, Q.; Maier, J.; Müllen, K. *Adv. Mater.* **2010**, *22*, 838–842.
(22) Yang, S.; Feng, X.; Ivanovici, S.; Müllen, K. *Angew. Chem., Int. Ed.* **2010**, *49*, 8408–8411.
(23) Wu, M. S.; Wang, M. J.; Jow, J. J. *J. Power Sources* **2010**, *195*, 3950–3955.
(24) Wang, Y.; Li, H.; He, P.; Hosono, E.; Zhou, H. *Nanoscale* **2010**, *2*, 1294–1305.
(25) Mattia, D.; Rossi, M. P.; Kim, B. M.; Korneva, G.; Bau, H. H.; Gogotsi, Y. *J. Phys. Chem. B* **2006**, *110*, 9850–9855.
(26) Zhang, Y. B.; Tan, Y. W.; Stormer, H. L.; Kim., P. *Nature* **2005**, *438*, 201–204.
(27) Novoselov, K. S.; Geim, A. K.; Morozov, S. V.; Jiang, D.; Katsnelson, M. I.; Grigorieva, I. V.; Dubonos, S. V.; Firsov, A. A. *Nature* **2005**, *438*, 197–200.
(28) Qiu, Y.; Yan, K.; Yang, S.; Jin, L.; Deng, H.; Li., W. *ACS Nano* **2010**, *4*, 6515–6526.
(29) Yoo, E.; Kim, J.; Hosono, E.; Zhou, H.; Kudo, T.; Honma, I. *Nano Lett.* **2008**, *8*, 2277–2282.
(30) Wang, H.; Cui, L. F.; Yang, Y.; Casalongue, H. S.; Robinson, J. T.; Liang, Y.; Cui, Y.; Dai, H. *J. Am. Chem. Soc.* **2010**, *132*, 13978–13980.
(31) Chou, S. L.; Wang, J. Z.; Choucair, M.; Liu, H. K.; Stride, J. A.; Dou, S. X. *Electrochem. Commun.* **2010**, *12*, 303–306.
(32) Zhang, M.; Lei, D.; Yin, X.; Chen, L.; Li, Q.; Wang, Y.; Wang, T. *J. Mater. Chem.* **2010**, *20*, 5538–5543.
(33) Wu, Z.; Ren, W.; Wen, L.; Gao, L.; Zhao, J.; Chen, Z.; Zhou, G.; Li, F.; Cheng, H. *ACS Nano* **2010**, *4*, 3187–3194.
(34) Yang, S.; Cui, G.; Pang, S.; Cao, Q.; Kolb, U.; Feng, X.; Maier, J.; Müllen, K. *ChemSusChem* **2010**, *3*, 236–239.
(35) Wang, B.; Wu, X. L.; Shu, C. Y.; Guo, Y. G.; Wang, C. R. *J. Mater. Chem.* **2010**, *20*, 10661–10664.
(36) Wang, J. Z.; Zhong, C.; Wexler, D.; Idris, N. H.; Wang, Z. X.; Chen, L. Q.; Liu, H. K. *Chem.—Eur. J.* **2010**, *17*, 661–667.
(37) Li, D.; Müller, M. B.; Gilje, S.; Kaner, R. B.; Wallace, G. G. *Nat. Nanotechnol.* **2008**, *3*, 101–105.
(38) Xu, Y. X.; Bai, H.; Lu, G. W.; Li, C.; Shi, G. Q. *J. Am. Chem. Soc.* **2008**, *130*, 5856–5857.
(39) Bae, D. S.; Han, K. S.; Cho, S. B.; Choi, S. H. *Mater. Lett.* **1998**, *37*, 255–258.
(40) Liu, H.; Wang, G. X.; Wang, J. Z.; Wexler, D. *Electrochem. Commun.* **2008**, *10*, 1879–1882.